



# Combination of structural and vascular optical coherence tomography for differentiating oral lesions of mice in different carcinogenesis stages

PING-HISEN CHEN,<sup>1,2,3</sup> CHIEN-HSIEN WU,<sup>3</sup> YI-FEN CHEN,<sup>4</sup> YI-CHEN YEH,<sup>5</sup>  
BO-HAN LIN,<sup>3</sup> KUO-WEI CHANG,<sup>4,6,7</sup> PEI-YU LAI,<sup>3</sup> MING-CHIH HOU,<sup>1,2,8</sup>  
CHING-LIANG LU,<sup>1,2</sup> AND WEN-CHUAN KUO<sup>3,\*</sup>

<sup>1</sup>Endoscopy Center for Diagnosis and Treatment, Taipei Veterans General Hospital, Taipei 112, Taiwan

<sup>2</sup>Faculty of Medicine, School of Medicine National Yang-Ming University School, Taipei 112, Taiwan

<sup>3</sup>Institute of Biophotonics, National Yang-Ming University, Taipei 112, Taiwan

<sup>4</sup>Institute of Oral Biology, National Yang-Ming University, Taipei 112, Taiwan

<sup>5</sup>Department of Pathology and Laboratory Medicine, Taipei Veterans General Hospital, Taipei 112, Taiwan

<sup>6</sup>Department of Dentistry, National Yang-Ming University, Taipei 112, Taiwan

<sup>7</sup>Department of Stomatology, Taipei Veterans General Hospital, Taipei 112, Taiwan

<sup>8</sup>Department of Medicine, Taipei Veterans General Hospital, Taipei 112, Taiwan

\*wckuo@ym.edu.tw

**Abstract:** Differentiating between early malignancy and benign lesions in oral cavities is difficult using current optical tools. As has been shown in previous studies, microvascular changes in squamous epithelium can be regarded as a key marker for diagnosis. We propose the combination of structural and vascular optical coherence tomography (OCT) imaging for the investigation of disease related changes. Progressive thickness changes of epithelium and the destruction of underlying lamina propria was observed during cancer development in a 4-nitroquinoline-1-oxide (4NQO) mouse model. At the same time, microvascular changes in hyperplasia, dysplasia, carcinoma in situ and advanced cancer were observed. Findings from OCT imaging were compared with histology.

© 2018 Optical Society of America under the terms of the [OSA Open Access Publishing Agreement](#)

**OCIS codes:** (170.0170) Medical optics and biotechnology; (110.4500) Optical coherence tomography.

## References and links

1. F. Bray, J. S. Ren, E. Masuyer, and J. Ferlay, "Global estimates of cancer prevalence for 27 sites in the adult population in 2008," *Int. J. Cancer* **132**(5), 1133–1145 (2013).
2. S. Warnakulasuriya, "Global epidemiology of oral and oropharyngeal cancer," *Oral Oncol.* **45**(4-5), 309–316 (2009).
3. M. McGurk, C. Chan, J. Jones, E. O'regan, and M. Sherriff, "Delay in diagnosis and its effect on outcome in head and neck cancer," *Br. J. Oral Maxillofac. Surg.* **43**(4), 281–284 (2005).
4. T. Amagasa, M. Yamashiro, and N. Uzawa, "Oral premalignant lesions: from a clinical perspective," *Int. J. Clin. Oncol.* **16**(1), 5–14 (2011).
5. S. S. Napier and P. M. Speight, "Natural history of potentially malignant oral lesions and conditions: an overview of the literature," *J. Oral Pathol. Med.* **37**(1), 1–10 (2008).
6. M. C. Downer, D. R. Moles, S. Palmer, and P. M. Speight, "A systematic review of test performance in screening for oral cancer and precancer," *Oral Oncol.* **40**(3), 264–273 (2004).
7. F. S. Mehta, P. C. Gupta, R. B. Bhonsle, P. R. Murti, D. K. Daftary, and J. J. Pindborg, "Detection of oral cancer using basic health workers in an area of high oral cancer incidence in India," *Cancer Detect. Prev.* **9**(3-4), 219–225 (1986).
8. K. A. Warnakulasuriya, A. N. Ekanayake, S. Sivayoham, J. Stjernsward, J. J. Pindborg, L. H. Sobin, and K. S. Perera, "Utilization of primary health care workers for early detection of oral cancer and precancer cases in Sri Lanka," *Bull. World Health Organ.* **62**(2), 243–250 (1984).
9. M. W. Lingen, J. R. Kalmar, T. Karrison, and P. M. Speight, "Critical evaluation of diagnostic aids for the detection of oral cancer," *Oral Oncol.* **44**(1), 10–22 (2008).
10. L. L. Patton, J. B. Epstein, and A. R. Kerr, "Adjunctive techniques for oral cancer examination and lesion diagnosis: a systematic review of the literature," *J. Am. Dent. Assoc.* **139**(7), 896–905, quiz 993–994 (2008).

11. D. Huang, E. A. Swanson, C. P. Lin, J. S. Schuman, W. G. Stinson, W. Chang, M. R. Hee, T. Flotte, K. Gregory, C. A. Puliafito, and et, "Optical coherence tomography," *Science* **254**(5035), 1178–1181 (1991).
12. M. Mogensen, L. Thrane, T. M. Joergensen, P. E. Andersen, and G. B. Jemec, "Optical coherence tomography for imaging of skin and skin diseases," *Semin. Cutan. Med. Surg.* **28**(3), 196–202 (2009).
13. S. C. Whiteman, Y. Yang, D. Gey van Pittius, M. Stephens, J. Parmer, and M. A. Spiteri, "Optical coherence tomography: real-time imaging of bronchial airways microstructure and detection of inflammatory/neoplastic morphologic changes," *Clin. Cancer Res.* **12**(3), 813–818 (2006).
14. B. E. Bouma, G. J. Tearney, C. C. Compton, and N. S. Nishioka, "High-resolution imaging of the human esophagus and stomach in vivo using optical coherence tomography," *Gastrointest. Endosc.* **51**(4), 467–474 (2000).
15. Z. Hamdoon, W. Jerjes, T. Upile, G. McKenzie, A. Jay, and C. Hopper, "Optical coherence tomography in the assessment of suspicious oral lesions: an immediate ex vivo study," *Photodiagn. Photodyn. Ther.* **10**(1), 17–27 (2013).
16. V. Volgger, H. Stepp, S. Ihrler, M. Kraft, A. Leunig, P. M. Patel, M. Susarla, K. Jackson, and C. S. Betz, "Evaluation of optical coherence tomography to discriminate lesions of the upper aerodigestive tract," *Head Neck* **35**(11), 1558–1566 (2013).
17. M. T. Tsai, C. K. Lee, H. C. Lee, H. M. Chen, C. P. Chiang, Y. M. Wang, and C. C. Yang, "Differentiating oral lesions in different carcinogenesis stages with optical coherence tomography," *J. Biomed. Opt.* **14**(4), 044028 (2009).
18. B. Davoudi, A. Lindenmaier, B. A. Standish, G. Allo, K. Bizheva, and A. Vitkin, "Noninvasive in vivo structural and vascular imaging of human oral tissues with spectral domain optical coherence tomography," *Biomed. Opt. Express* **3**(5), 826–839 (2012).
19. W. J. Choi and R. K. Wang, "In vivo imaging of functional microvasculature within tissue beds of oral and nasal cavities by swept-source optical coherence tomography with a forward/side-viewing probe," *Biomed. Opt. Express* **5**(8), 2620–2634 (2014).
20. C. L. Chen and R. K. Wang, "Optical coherence tomography based angiography [Invited]," *Biomed. Opt. Express* **8**(2), 1056–1082 (2017).
21. H. Inoue, M. Kaga, H. Ikeda, C. Sato, H. Sato, H. Minami, E. G. Santi, B. Hayee, and N. Eleftheriadis, "Magnification endoscopy in esophageal squamous cell carcinoma: a review of the intrapapillary capillary loop classification," *Ann. Gastroenterol.* **28**(1), 41–48 (2015).
22. A. Vu and C. S. Farah, "Narrow band imaging: clinical applications in oral and oropharyngeal cancer," *Oral Dis.* **22**(5), 383–390 (2016).
23. M. Contaldo, A. Lucchese, E. Gentile, C. Zulli, M. Petrucci, D. Lauritano, M. R. Amato, P. Esposito, G. Riegler, and R. Serpico, "Evaluation of the intraepithelial papillary capillary loops in benign and malignant oral lesions by in vivo Virtual Chromoendoscopic Magnification: a preliminary study," *J. Biol. Regul. Homeost. Agents* **31**(2 Suppl 1), 11–22 (2017).
24. C. Jiang, D. Ye, W. Qiu, X. Zhang, Z. Zhang, D. He, P. Zhang, and W. Chen, "Response of lymphocyte subsets and cytokines to Shenyang prescription in Sprague-Dawley rats with tongue squamous cell carcinomas induced by 4NQO," *BMC Cancer* **7**(1), 40 (2007).
25. M. Vered, I. Allon, A. Buchner, and D. Dayan, "Stromal myofibroblasts and malignant transformation in a 4NQO rat tongue carcinogenesis model," *Oral Oncol.* **43**(10), 999–1006 (2007).
26. R. N. Silva, D. A. Ribeiro, D. M. Salvadori, and M. E. Marques, "Placental glutathione S-transferase correlates with cellular proliferation during rat tongue carcinogenesis induced by 4-nitroquinoline 1-oxide," *Exp. Toxicol. Pathol.* **59**(1), 61–68 (2007).
27. N. W. Chang, R. J. Pei, H. C. Tseng, K. T. Yeh, H. C. Chan, M. R. Lee, C. Lin, W. T. Hsieh, M. C. Kao, M. H. Tsai, and C. F. Lin, "Co-treating with arecoline and 4-nitroquinoline 1-oxide to establish a mouse model mimicking oral tumorigenesis," *Chem. Biol. Interact.* **183**(1), 231–237 (2010).
28. X. H. Tang, B. Knudsen, D. Bemis, S. Tickoo, and L. J. Gudas, "Oral cavity and esophageal carcinogenesis modeled in carcinogen-treated mice," *Clin. Cancer Res.* **10**(1), 301–313 (2004).
29. Y. F. Chen, C. C. Yang, S. Y. Kao, C. J. Liu, S. C. Lin, and K. W. Chang, "MicroRNA-211 Enhances the Oncogenicity of Carcinogen-Induced Oral Carcinoma by Repressing TCF12 and Increasing Antioxidant Activity," *Cancer Res.* **76**(16), 4872–4886 (2016).
30. T. H. Chu, C. C. Yang, C. J. Liu, M. T. Lui, S. C. Lin, and K. W. Chang, "miR-211 promotes the progression of head and neck carcinomas by targeting TGF $\beta$ RII," *Cancer Lett.* **337**(1), 115–124 (2013).
31. W. C. Kuo, C. M. Lai, Y. S. Huang, C. Y. Chang, and Y. M. Kuo, "Balanced detection for spectral domain optical coherence tomography," *Opt. Express* **21**(16), 19280–19291 (2013).
32. H. Lin, M. C. Kao, C. M. Lai, J. C. Huang, and W. C. Kuo, "All fiber optics circular-state swept source polarization-sensitive optical coherence tomography," *J. Biomed. Opt.* **19**(2), 021110 (2013).
33. G. Liu, W. Jia, V. Sun, B. Choi, and Z. Chen, "High-resolution imaging of microvasculature in human skin in-vivo with optical coherence tomography," *Opt. Express* **20**(7), 7694–7705 (2012).
34. S. Yousefi, J. Qin, Z. Zhi, and R. K. Wang, "Label-free optical lymphangiography: development of an automatic segmentation method applied to optical coherence tomography to visualize lymphatic vessels using Hessian filters," *J. Biomed. Opt.* **18**(8), 086004 (2013).
35. W. E. Hart, M. Goldbaum, B. Côté, P. Kube, and M. R. Nelson, "Measurement and classification of retinal vascular tortuosity," *Int. J. Med. Inform.* **53**(2-3), 239–252 (1999).

36. X. Liu, N. Xu, and A. Jiang, "Tortuosity entropy: a measure of spatial complexity of behavioral changes in animal movement," *J. Theor. Biol.* **364**, 197–205 (2015).
37. P. Wilder-Smith, K. Lee, S. Guo, J. Zhang, K. Osann, Z. Chen, and D. Messadi, "In vivo diagnosis of oral dysplasia and malignancy using optical coherence tomography: preliminary studies in 50 patients," *Lasers Surg. Med.* **41**(5), 353–357 (2009).
38. M. T. Tsai, H. C. Lee, C. W. Lu, Y. M. Wang, C. K. Lee, C. C. Yang, and C. P. Chiang, "Delineation of an oral cancer lesion with swept-source optical coherence tomography," *J. Biomed. Opt.* **13**(4), 044012 (2008).
39. W. Wei, W. J. Choi, and R. K. Wang, "Microvascular imaging and monitoring of human oral cavity lesions in vivo by swept-source OCT-based angiography," *Lasers Med. Sci.* **33**(1), 123–134 (2018).
40. M. J. Girard, N. G. Strouthidis, C. R. Ethier, and J. M. Mari, "Shadow removal and contrast enhancement in optical coherence tomography images of the human optic nerve head," *Invest. Ophthalmol. Vis. Sci.* **52**(10), 7738–7748 (2011).

## 1. Introduction

Oral cancer is the 11th most common cancer in the world, accounting for an estimated 300,000 new cases, 145,000 deaths in 2012, and 702,000 prevalent cases over a period of five years [1]. Despite the advancement in targeted cancer therapy, survival rate for oral cancer has remained flat for the last 50 years [2]. The most important determining factor is the diagnostic stage, but up to 50% of oral cancers are not detected until the disease is quite advanced [3]. From the pathogenesis of oral cancer, approximately 95% of oral cancer is squamous cell carcinoma (SCC) with a long preclinical phase, consisting of well-documented precancerous lesions, called oral potentially malignant disorder (OPMD). These include homogeneous leukoplakia, nonhomogeneous leukoplakia, verrucous leukoplakia, erythroplakia, oral submucous fibrosis, lichen planus, and chronic traumatic ulcers. The estimated annual frequency of malignant transformation of OPMD ranged from 0.13 to 2.2% and would experience the sequential course of hyperplasia, dysplasia, and carcinoma in situ (CIS) to invasive SCC [4,5]. Therefore, it is reasonable that oral cancer can be diagnosed and treated in the pre- or early-malignant stages.

A conventional visual examination is the most commonly used screening program for detecting oral cancer, but the accuracy varies in different studies (sensitivity 40–94%, specificity 50–99%) [6–8]. The use of adjunctive aids, such as, toluidine blue, diffuse white light, chemiluminescence, or loss of tissue autofluorescence has been studied, but there is not yet sufficient evidence to justify their effectiveness [9,10]. To date, accurately predicting the malignant transformation of OPMDs displaying dysplasia is not possible under current diagnostic tools. The use of non-invasive real time optical imaging systems to obtain an optical biopsy and diagnose malignancies early is an active research area. Optical coherence tomography (OCT) is especially a rapidly developing tool [11]. OCT provides real-time and high-resolution (10–20  $\mu\text{m}$ ) cross-sectional images with a penetration depth of 1–2 mm. The clinical applications of OCT have expanded to involve a wide range of clinical domains [12–14]. In the oral cavity, studies have attempted to use OCT to differentiate benign or early malignant lesions via different structural or optical markers, including the thickness of the epithelium, the intactness of basement membrane, intraepithelial intensity reduction, or optical scattering properties; however, these studies were controversial and were not clinically useful [15–17].

Doppler OCT is a blood flow detection method that measures the phase change of the back-scattered light from red blood cells and quantifies flow speed. Recently, studies have successfully used Doppler OCT to investigate microvasculature in the healthy human oral cavity [18,19]. In order to visualize microvasculature, OCT angiography methods can be used that rely on amplitude or phase variance between successive measurements (e.g., cross-sectional images). Amplitude variance is the preferred method in the case of unstable phase situations, such as, swept-source OCT [20]. The microvascular change in squamous epithelium, called intraepithelial papillary capillary loop (IPCL), is the most specific optical marker for differentiating benign or malignant lesions in esophageal SCC [21]. Recently, some studies have shown that magnifying endoscopy with a narrow-band image to evaluate

IPCLs in the oral cavity can improve detection rates of OPMD and can better assess benign or malignant lesions [22,23]. However, clinical applications of this method in the oral cavity are still limited because of the complex anatomy of the oral cavity, the difficulty of endoscope operation, hyperkeratosis of the oral lesion, and interference from mucous and salivary secretions.

OCT can provide better resolution and deeper penetration than a current magnifying endoscope. As OCT is a non-contact method, difficulties in system operation can be overcome. In this pioneer animal study, we used structural OCT and OCT angiography to investigate progressive disease-related changes in different carcinogenesis stages of oral SCC. The results of this study indicate that the system can differentiate between benign and early-malignant oral lesions.

## 2. Experimental methods

### 2.1 Animal model and protocol

4-Nitroquinoline-1-oxide (4NQO) is a water-soluble quinoline derivative that forms DNA adducts and induces intracellular oxidative stress, resulting in mutations and DNA strand breaks. This process is similar to the genetic alterations provoked by tobacco exposure. This is a powerful carcinogen in several organs, and it can induce tongue SCC when applied in low concentrations via drinking water. The resulting sequential changes and morphological features resemble those seen during the progression of human tongue SCC, including the progression from hyperplasia and dysplasia to SCC. These occurred within 28 weeks [24–27]. This model is the best available experimental system for investigating the progression of early oral cancer [28].

The K14-miR-211-GFP transgenic mice used in this study were established by Chang et al. [29]. This model has a higher potential for tumor development after 4NQO induction than wild mice, and the developed tumors with intensified green fluorescence are identified easily by the fluorescent system. To induce tumorigenesis, 100  $\mu\text{g/mL}$  of the water-soluble carcinogen 4NQO (Sigma-Aldrich, St. Louis, MO, USA) was added to the drinking water of 6-week-old K14-miR-211-GFP transgenic mice for 12 weeks [28,30].

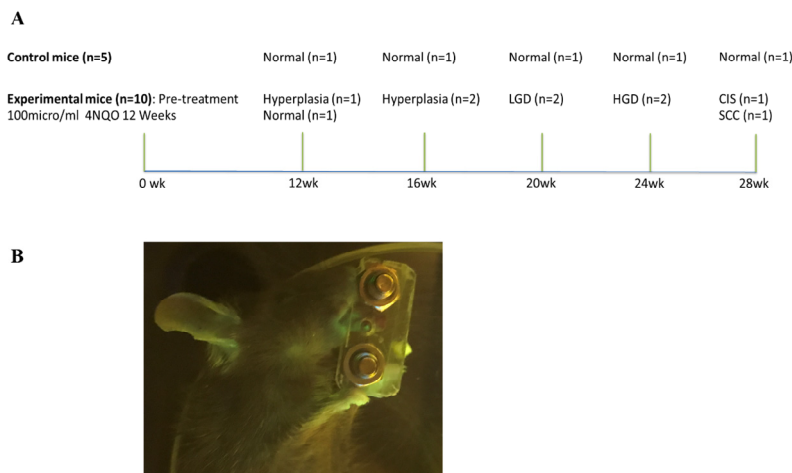


Fig. 1. Imaging protocol. (A) OCT imaging schedule and time of mouse sacrifice for histology. (B) Fluorescent image of the tongue: the green spot indicated the potential tumor location on the dorsal surface of the tongue and was fixed by two plastic slides with a 2mm diameter hole before OCT imaging.

Overall, ten experimental mice receiving 4NQO induction and five control mice without 4NQO exposure were studied. OCT imaging was performed on the 12th, 16th, 20th, 24th, and

28th week after induction start. Two experimental mice and one control mouse were studied at each scheduled time (Fig. 1(A)). Before OCT scanning, the mouse was anesthetized by intraperitoneal injection of 2,2,2 tribromoethanol (200 mg/kg), then the tongue was scanned with a fluorescent system (LT-9900 Illumatool bright light). A green spot on the surface of the dorsal tongue indicated a potential tumor position. The location was positioned between two plastic slides with a 2-mm-diameter central hole (Fig. 1(B)). The OCT imaging was then performed around this area. Following the OCT scanning, the mouse was sacrificed, and the tongue tissue was resected, inked, fixed, and processed for histopathological analysis. The study was approved by the Institution for Animal Care and Use Committee at National Yang-Ming University.

## 2.2 Setup of OCT

The design of our OCT imaging system was based on spectral-domain OCT. The light source was a supercontinuum laser with a central wavelength of 1275 nm and a spectral bandwidth of 200 nm. A 50/50 coupler was arranged to split the light power into 50% for the reference mirror (with an attenuator) and 50% incident power (i.e., ~6 mW) focused to a scanning spot. After the recombination of the sample and reference beams, the light was sent to a line-scan spectrometer (2048 pixels, Wasatch Photonics) for detection, and the data were transferred to a computer. After the data acquisition, resampling from  $\lambda$  to a specified  $k$  space was performed on each spectrum to ensure the spectrum was linearly interpolated in  $k$ -space [31]. Then, dispersion compensation was used to ensure the signal could be accurately recovered to the depth profile after fast Fourier transform (FFT) of the spectral interferogram [32]. The image acquisition rate, 76 frames per second ( $1000 \times 1024$  pixels in the X-Z plane), was based on the setting of integration time in a line-scan spectrometer and the scanning speed of the X-Y galvanometer scanner. The axial system resolution in air was measured ~5  $\mu\text{m}$  after dispersion compensation by using a mirror with an attenuator as a sample. As for measurement of the lateral resolution, a 1951 USAF resolution test target (Edmund Optics) was used as the standard resolution test sample, confirming that the lateral resolution of the OCT setup was approximately 7  $\mu\text{m}$ .

## 2.3 Vascular OCT image analysis

After acquisition of the spectral interferograms, structural images and vascular images were calculated. The intensity images were displayed on a logarithmic grayscale. The vascular images were calculated via amplitude variance. To determine the microstructure of the tongue tissues, a three-dimensional (3D) data set consisting of 1800 two-dimensional (2D) OCT images were recorded covering a volume of  $3 \text{ mm} \times 3 \text{ mm} \times 3 \text{ mm}$  corresponding to  $1000 \times 1800 \times 1024$  pixels in the X, Y, and Z directions. Different viewing angles can be reconstructed by 3D visualization framework software (Avizo 6.1). By calculating the amplitude term in the autocorrelation algorithm between B-scans (i.e., inter-frame calculation), the coefficient value can be written as

$$\sigma^2 = 1 - \frac{\sum_{y_j=1}^J \sum_{z=1}^N |A_{x,y_j,z}| |A_{x,y_{j+1},z}|}{\sum_{y_j=1}^J \sum_{z=1}^N \left( \frac{|A_{x,y_j,z}|^2 + |A_{x,y_{j+1},z}|^2}{2} \right)} \quad (1)$$

Here,  $x$ ,  $y$ , and  $z$  are the spatial pixel coordinates corresponding to the fast and slow scanning axis and the depth coordinate, respectively.  $|A_{x,y_j,z}|$  is the amplitude of the complex-value OCT data of the  $j$ th B-scan.  $J = 4$  is the number of averaged B-scans, and  $N = 4$  is the number of averaged depth pixels. Vascular contrast is achieved, because flow regions and bulk tissue



give very different correlation values. Complete mathematical descriptions are provided in the references [33].

The OCT angiography images were filtered by a 2D Hessian filter [34], and then were manually divided into a superficial mucosal layer and a deep mucosal layer according to the boundary of the epithelium (EP) and lamina propria (LP) in the OCT intensity images. This was used to compare with the current IPCL image presented via the magnifying endoscope with a narrow-band image [21]. The maximum intensity projection from the tissue surface to the imaging depth was used to study vessel morphology in a depth range and is presented in a 2D en-face image (XY plane). In quantitative analysis, three parameters were automatically calculated using a program written in MATLAB (MathWorks). First, vessel area density was defined as the area of the vessels in the projection view divided by the area of the imaging region. Second, by using the Euclidean distance transform [34] of the binarized vessel en-face projection map, the distance between each pixel in a binarized map to the pixel locations that approximate the center line of the blood vessels (i.e., vessel skeleton) was counted in pixel number, and then averaged as vessel median diameter. Third, bendiness was determined by calculating the vessel tortuosity [35] of the skeletonized vessel en-face projection map. Larger tortuosity entropy corresponds to a more tortuous and “wiggly” vessel trajectory [36].

#### 2.4 Histological analysis

The fixed samples were later embedded in paraffin, sectioned, and stained with hematoxylin and eosin for histopathological analysis. The histological change was assessed by an experienced pathologist, and the result was classified into one of the following categories: (1) normal, (2) hyperplasia to low-grade dysplasia (LGD), (3) high-grade dysplasia (HGD) to CIS, and (4) SCC.

### 3. Results

#### 3.1 Animals and histological results

The progression of tongue cancer in ten experimental mice is shown in Fig. 1(A). Overall, one mouse showed normal histology, five mice developed hyperplasia to LGD, three mice developed HGD to CIS, and one mouse developed SCC in the experimental group. All five control mice showed normal histology at all times (Fig. 1(A)).

#### 3.2 In vivo structural and vascular imaging of the anterior, dorsal tongue of a control mouse

Figure 2(A) shows a 3D-rendered OCT structural image of the anterior dorsal tongue of a control mouse. Figure 2(B) shows a cross-sectional image that was recorded at a location indicated with the green dotted line in Fig. 2(A). This describes typical tongue anatomical features: a filiform papilla (FiPa), a keratinized layer (KL), an epithelial layer (EP), and an underlying lamina propria (LP). Shadowing artifacts originating from the papilla structure are also observed. The corresponding histological image is shown in Fig. 2(C). Figure 2(D) is the vascular image corresponding to the orange rectangle in Fig. 2(B), which demonstrates that a small IPCLs (orange arrow) rose perpendicularly from the branching vessel network into the junction of the EP and LP, and large branching vessels (green arrow) that ran in the LP. To visualize the vessel networks in depth, the vascular image data sets were collected over the superficial mucosal layer (above the junction of EP and LP) and the deep mucosal layer (below the junction of EP and LP). These were reconstructed into a 2D en-face (XY) image as shown in Figs. 2(E) and 2(G).

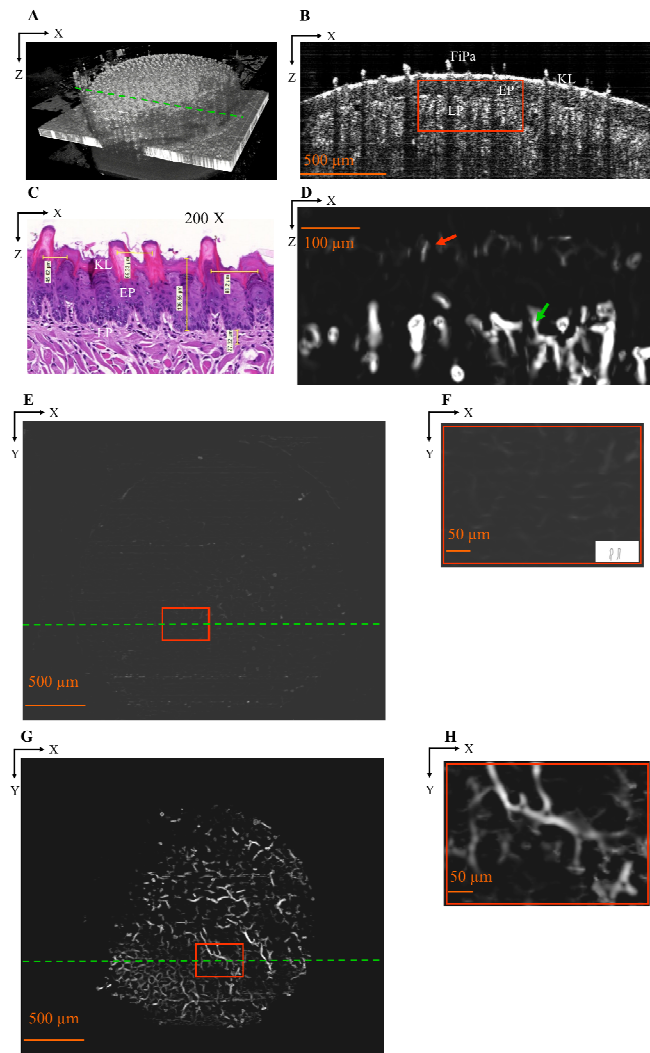


Fig. 2. In vivo structural and vascular imaging of the anterior, dorsal tongue of control mouse. (A) 3D rendered OCT structural image. (B) Cross-sectional OCT image at the location of the green dotted line in (A). (C) Histological image of approximately the same location as displayed in (B). (D) Corresponding vascular image from the orange rectangle in (B) (orange arrow: IPCL in the junction of EP and LP; green arrow: branching vessels in the LP). (E) 2D en-face vascular image of superficial mucosal layer showing IPCL. (F) Magnified image of region indicated with orange rectangle in (E) showing small and narrow IPCL. (G) 2D en-face vascular image in deep mucosal layer showing branching vessels in LP. (H) Magnified image of branching vessels indicated with orange rectangle in (G). IPCL: intraepithelial papillary capillary loops; KL: keratinized layer; FiPa: filiform papilla; EP: epithelial layer; LP: lamina propria.

Figure 2(E) presents a 2D en-face vascular image of the superficial mucosal layer showing a representative IPCLs. There are few IPCLs in this figure, because the small size of a normal IPCL (approximately 5–10  $\mu\text{m}$ ) falls below the spatial resolution of our system; shadowing artifacts originating from the papilla of a normal tongue also influence the image quality. Figure 2(F) is a magnified image of IPCLs from the orange rectangle in Fig. 2(E). This shows the IPCLs as a small and closed loop more clearly. By calculating how many successive B-scans show individual loop signals, the smallest detectable IPCL is estimated at approximately 10  $\mu\text{m}$  (width). At deeper depths, Fig. 2(G) presents a 2D en-face vascular

image in the deep mucosal layer including representative branching vessels. Figure 2(H) is a magnified image of branching vessels from the orange rectangle in Fig. 2(G). Because the morphology of branching vessels is difficult to define, further quantitative analysis in Fig. 2(G) was performed; it shows the vessel area density, median diameter, and bending of branching vessels are 0.116, 1.462 and 0.272.

### 3.3 *In vivo structural and vascular imaging of the dorsal tongue with hyperplasia to LGD of a 4NQO mouse*

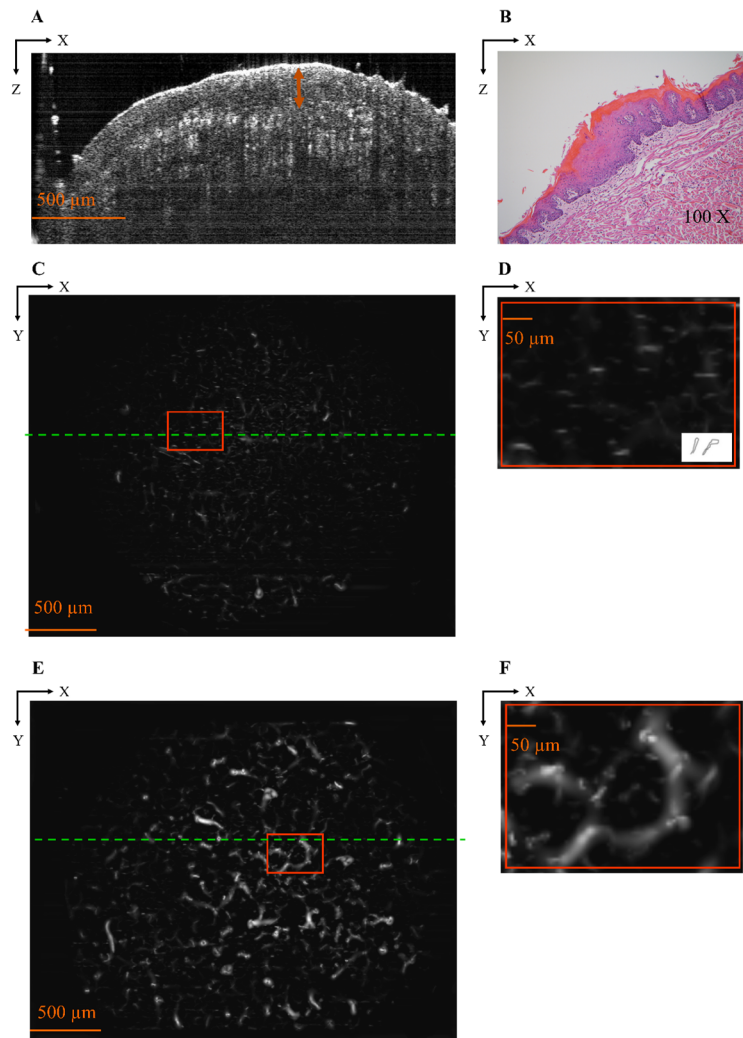


Fig. 3. In vivo Structural and Vascular imaging of the dorsal tongue with hyperplasia to LGD of 4NQO mouse. (A) Cross-sectional OCT image at the location of the green dotted line in (C) shows increased thickness of the EP (orange double-sided arrow) with the preserved boundary of EP and LP. (B) Corresponding histology image obtained at a similar location as displayed in (A) which shows increased thickness of EP with basal cell hyperplasia. (C) 2D en-face vascular image of superficial mucosal layer showing IPCL. (D) Magnified image of region indicated with orange rectangle in (C). IPCL presents as elongated and closed loops. (E) 2D en-face vascular image of deep mucosal layer showing branching vessels in LP. (F) Magnified image of region indicated with orange rectangle in (E). IPCL: intraepithelial papillary capillary loop; EP: epithelial layer; LP: lamina propria; LGD: low grade dysplasia.



Figure 3(A) shows a cross-sectional image that was recorded at a location indicated with the green dotted line in Fig. 3(C). Increased thickness of the EP (orange double-sided arrow) with the preserved boundary of EP and LP can be observed. The corresponding histological image is shown in Fig. 3(B) and shows an increased thickness of the epithelium layer with basal cell hyperplasia. Figure 3(C) shows a 2D en-face vascular image in the superficial mucosal layer including a representative IPCL. Figure 3(D) is a magnified image of IPCLs at a location indicated by the orange rectangle in Fig. 3(C). This presents IPCLs with an elongated and closed loop (approximately 15–20  $\mu\text{m}$ ). At deeper depths, Fig. 3(E) presents a 2D en-face vascular image in the deep mucosal layer including representative branching vessels. Figure 3(F) is a magnified image of branching vessels at a location indicated by the orange rectangle in Fig. 3(E). The quantitative analysis in Fig. 3(E) shows that the area density, median diameter, and bending of branching vessels are 0.137, 1.729 and 0.277.

#### ***3.4 In vivo structural and vascular imaging of the dorsal tongue with HGD to CIS of a 4NQO mouse***

Figure 4(A) shows a cross-sectional image that was recorded at a location indicated with the green dotted line in Fig. 4(C). Increased thickness of EP (indicated by orange double-sided arrow) with preserved boundary of EP and LP can be observed. The corresponding histological image is shown in Fig. 4(B); it shows the full thickness of the dysplastic changes in the lining epithelium. Figure 4(C) presents a 2D en-face vascular image in the superficial mucosal layer including a representative IPCL. Figure 4(D) is a magnified image of IPCLs at a location indicated by the orange rectangle in Fig. 4(C). It shows IPCLs with open, dilated, meandering, and non-uniform loops (approximately 25–35  $\mu\text{m}$ ). At the deeper depths, Fig. 4(E) presents 2D en-face vascular images in the deep mucosal layer including representative branching vessels. Figure 4(F) is a magnified image of branching vessels at a location indicated by the orange rectangle in Fig. 4(E). The quantitative analysis in Fig. 4(E) shows that the area density, median diameter, and bending of branching vessels in Fig. 4(E) are 0.228, 1.550 and 0.311.

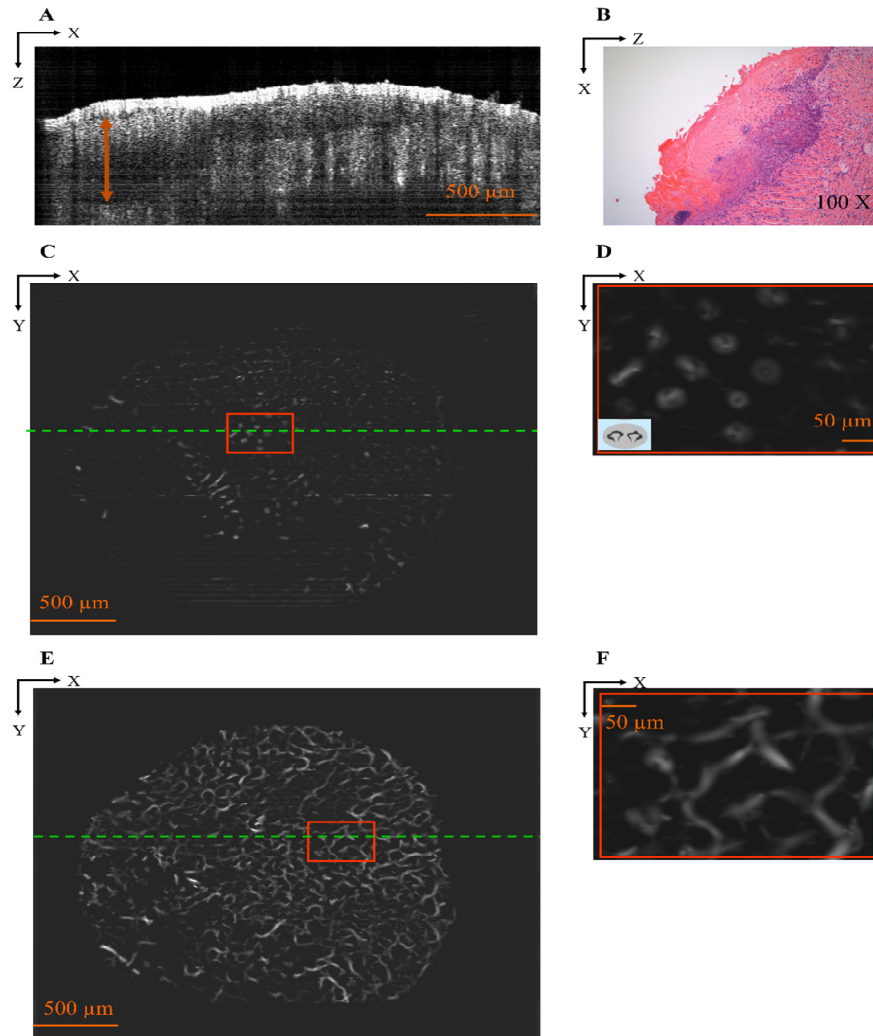


Fig. 4. *In vivo* structural and vascular imaging of the dorsal tongue with HGD to CIS of 4NQO mouse (A) Cross-sectional OCT image at the location of the green dotted line in (C) shows increased thickness of the EP (orange double-sided arrow) with the preserved boundary of EP and LP. (B) Corresponding histology image obtained at a similar location as displayed in (A) which shows full thickness of dysplastic changes of the lining epithelium. (C) 2D en-face vascular image of superficial mucosal layer showing IPCL. (D) Magnified image of region indicated with orange rectangle in (C). IPCL presents as open, dilated, meandering, and non-uniform loops. (E) 2D en-face vascular image of deep mucosal layer showing branching vessels in LP. (F) Magnified image of region indicated with orange rectangle in (E). IPCL: intraepithelial papillary capillary loop; EP: epithelial layer; LP: lamina propria; HGD: high grade dysplasia; CIS: carcinoma in situ.

### 3.5 Comparing IPCLs between hyperplasia to LGD and HGD to CIS

This mouse was examined at week 28. Before OCT scanning, multifocal green lesions are observed on the fluorescent image. Therefore, we enlarged the scanning area to  $3 \times 4$  mm (x and y axes) to cover these lesions at the same time; the result is shown in Fig. 5. Figure 5(A) is a 2D en-face vascular image in the superficial mucosal layer including a representative IPCL. A cross-sectional image at the location indicated by the blue dotted line in Fig. 5(A) is shown in Fig. 5(B). An increased thickness of the EP (orange double-sided arrow) with the

preserved boundary of EP and LP can be observed. The corresponding histological image is shown in Fig. 5(C), and the expert grader indicated a hyperplasia to LGD change. Figure 5(D) is a magnified image of IPCLs at a location indicated by the blue rectangle in Fig. 5(A). This shows IPCLs with an elongated and closed loop as shown in Fig. 3(D), indicating hyperplasia to LGD change.

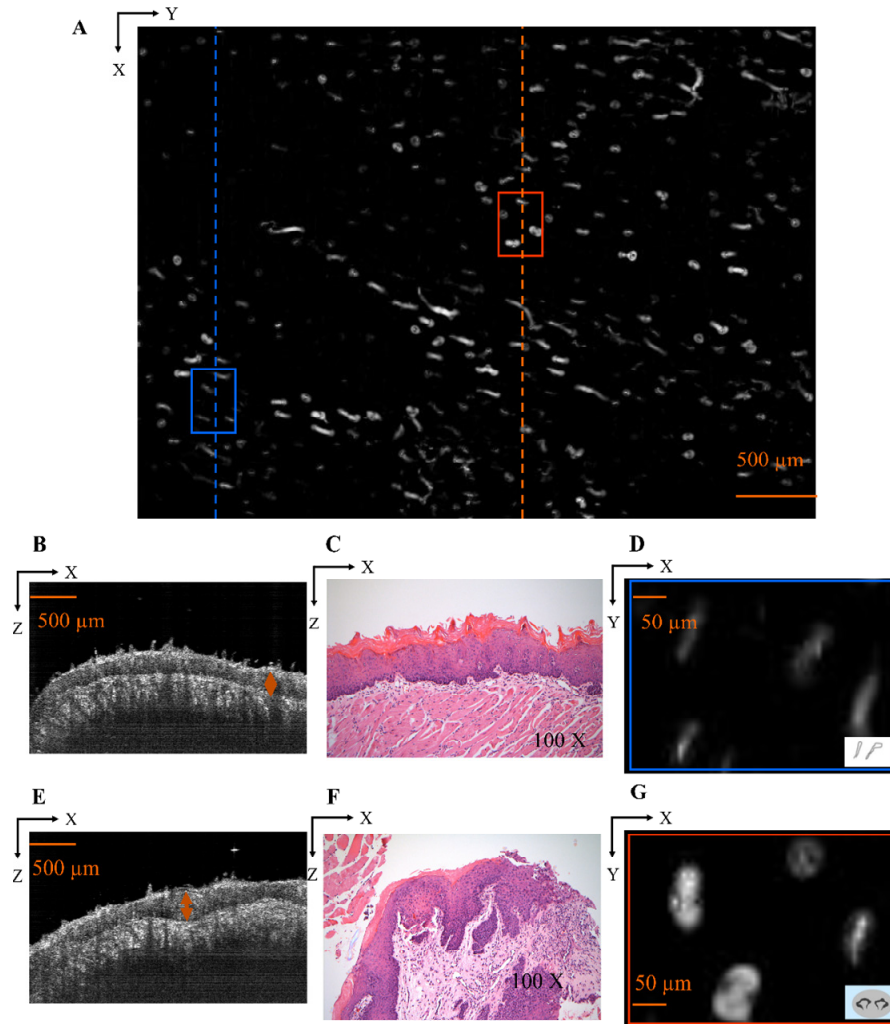


Fig. 5. Comparing IPCL between hyperplasia to LGD and HGD to CIS. (A) 2D en-face vascular image of superficial mucosal layer showing IPCL. (B) Cross-sectional OCT image at the location of the blue dot line in (A) shows increased thickness of the EP (orange double-sided arrow) with the preserved boundary of EP and LP. (C) Corresponding histology image obtained at a similar location as displayed in (B) which indicates hyperplasia to LGD. (D) Magnified image of IPCL indicated with the blue rectangle in (A). It presents IPCL with elongated and closed loop, favor hyperplasia to LGD change. (E) Cross-sectional OCT image at the location of the orange dot line in (A) shows focal thickness of the EP (orange double-sided arrow) with the preserved boundary of EP and LP layer. (F) Corresponding histology image obtained at a similar location as displayed in (E) which indicates HGD to CIS change. (G) Magnified image of IPCL indicated with the orange rectangle in (A). It presents IPCL with opened, dilated, meandering, and non-uniform loop, favor HGD to CIS change. IPCL: intraepithelial papillary capillary loop; EP: epithelial layer; LP: lamina propria; LGD: low grade dysplasia; HGD: high grade dysplasia; CIS: carcinoma in situ.

In the other area, a cross-sectional image at the location indicated by the orange dotted line in Fig. 5(A) is shown in Fig. 5(E). This shows a focal thickness of the EP layer (orange double-sided arrow) with a preserved boundary between the EP and LP layers. The corresponding histological image is shown in Fig. 5(F), and the expert grader indicated an HGD to CIS change. Figure 5(G) is a magnified image of IPCLs at a location indicated by the orange rectangle in Fig. 5(A). This presents IPCLs with open, dilated, meandering, and non-uniform loops as shown in Fig. 4(D). This indicates an HGD to CIS change. It is difficult to differentiate these two pathological processes (benign vs. early malignant) by the structural image, because all images show a focal epithelial thickness with a preserved boundary between the EP and LP layers; however, this distinction is easily achieved with vascular images.

### 3.6 Comparing IPCLs between HGD to CIS and SCC

Figure 6 shows another mouse that has multifocal green lesions before OCT scanning. We also enlarged the scanning area to  $3 \times 4$  mm to cover these lesions at the same time. Figure 6(A) is a 2D en-face vascular image in a superficial mucosal layer including representative IPCL. A cross-sectional image at the location of the blue dotted line in Fig. 6(A) is shown in Fig. 6(B). An increased thickness of the EP (orange double-sided arrow) with a preserved boundary of EP and LP layers can be observed. The corresponding histological image is shown in Fig. 6(C), and the expert grader indicated HGD to CIS. Figure 6(D) is a magnified image of IPCLs at a location indicated by the blue rectangle in Fig. 6(A). It presents IPCLs with open, dilated, meandering, and non-uniform loops as shown in Fig. 4(D). This indicates an HGD to CIS change.

In the other area, a cross-sectional image at the location of the orange dotted line in Fig. 6(A) is shown in Fig. 6(E). This presents a polypoid tumor with an LP layer invasion (orange arrow). The corresponding histological image is shown in Fig. 6(F), and the expert grader indicated SCC with muscular-layer invasion. Figure 6(G) is a magnified image of IPCL at a location indicated by the orange rectangle in Fig. 6(A). It presents large and branching neovascular tumor vessels, indicating advanced SCC change. It is easy to differentiate early malignant lesion and SCC by structural and vascular imaging at the same time.

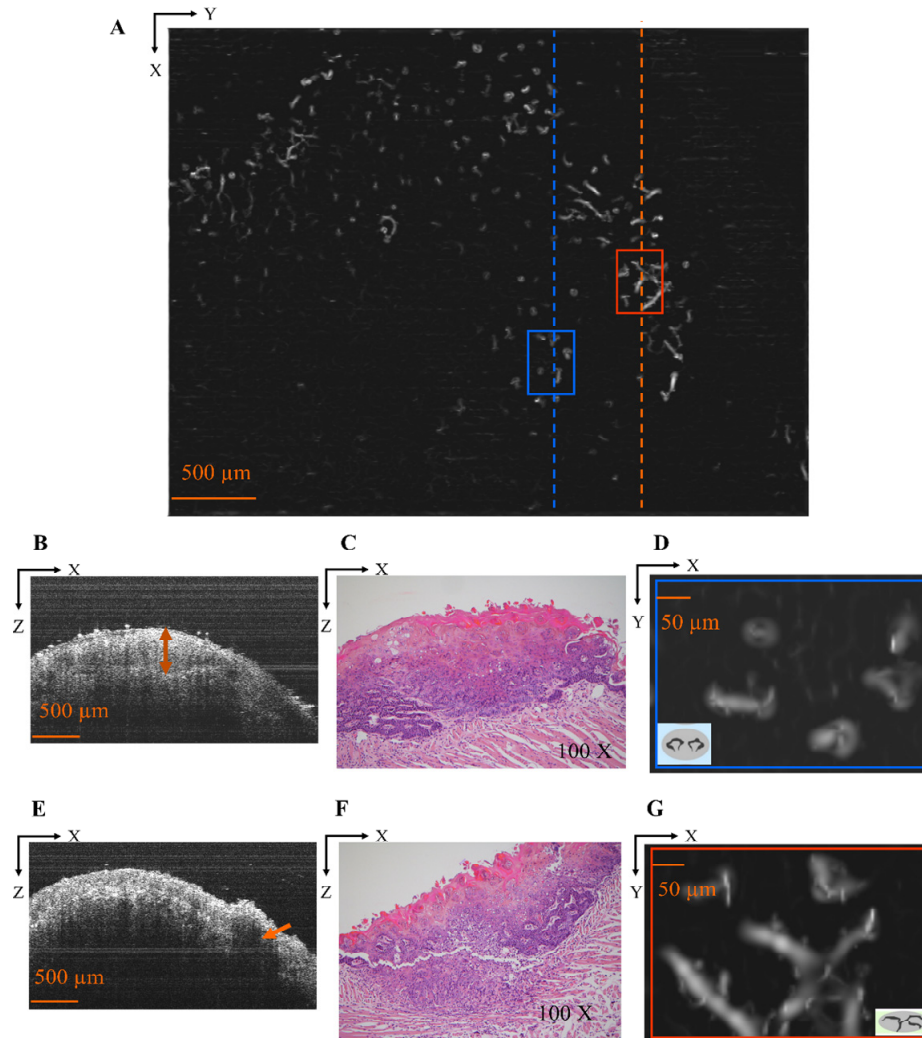


Fig. 6. Comparing IPCL between HGD to CIS and SCC (A) 2D en-face vascular image of superficial mucosal layer showing IPCL. (B) Cross-sectional OCT image at the location of the blue dot line in (A) shows increased thickness of the EP with the preserved boundary of EP and LP layer (orange double-sided arrow). (C) Corresponding histology image obtained at a similar location as displayed in (B) which indicates HGD to CIS change. (D) Magnified image of IPCL indicated with the blue rectangle in (A). It presented IPCL with open, dilated, meandering, and non-uniform loop, favor HGD to CIS change. (E) Cross-sectional OCT image at the location of the orange dot line in (A) shows polypoid tumor with LP layer invasion (orange arrow). (F) Corresponding histology image obtained at a similar location as displayed in (E) which indicates SCC with muscular layer invasion. (G) Magnified image of IPCL indicated with the orange rectangle in (A). It presented large branching type neovascular tumor vessels, favor advanced SCC change. IPCL: intraepithelial papillary capillary loop; EP: epithelial layer; LP: lamina propria; HGD: high grade dysplasia; CIS: carcinoma in situ; SCC: squamous cell carcinoma.

### 3.7 Progression of structural and vascular images in different pathological processes

Figure 7 shows the change in structure and vasculature from normal (Fig. 7(A)), hyperplasia to LGD (Fig. 7(B)), HGD to CIS (Fig. 7(C)), to SCC (Fig. 7(D)). It is easy to differentiate SCC and other benign or early malignant lesions via the structural image because of the invasion of the LP layer (Fig. 7(D)). However, it becomes difficult to differentiate between



hyperplasia or early malignant lesions, because the only observed features in a structural image are the thickness of the EP layer (Figs. 7(B) and 7(C)). IPCLs are helpful to aid in the diagnosis. We can see the progression of IPCLs from the small and closed loop (normal, Fig. 7 (A)), elongated and closed loop (hyperplasia to LGD, Fig. 7(B)), open and dilated loop (HGD to CIS, Fig. 7(C)), and finally to the large and branching vessels (SCC, Fig. 7(D)).

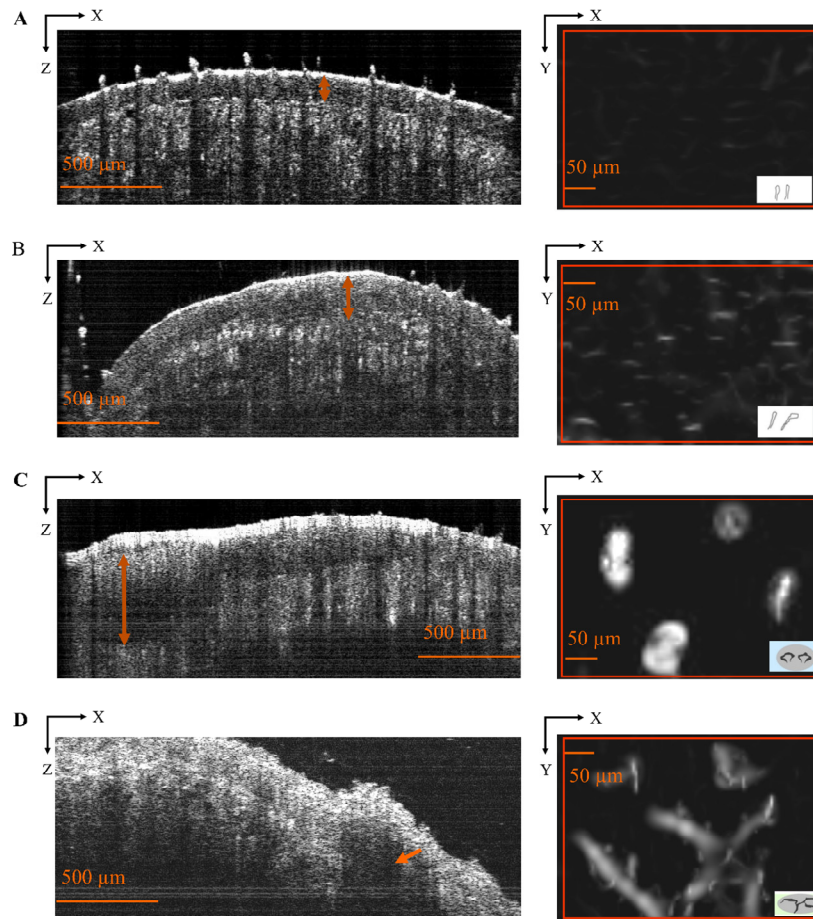


Fig. 7. Change of structure and vasculature in different pathological stages of disease progression. (A) normal histology: normal structural image (left part) with small and closed IPCL (right part). (B) hyperplasia to LGD: focal thickness of EP layer (left part) with elongated and closed IPCL (right part). (C) HGD to CIS: focal thickness of EP layer (left part) with open, dilated and meandering IPCL (right part). (D) SCC: polypoid tumor with LP invasion (left part) with large and branching IPCL (right part). IPCL: intraepithelial papillary capillary loop; EP: epithelial layer; LP: lamina propria; LGH: low grade dysplasia; HGD: high grade dysplasia; CIS: carcinoma in situ; SCC: squamous cell carcinoma.

#### 4. Discussion and conclusion

This was, to the best of our knowledge, the first study to combine structural and vascular OCT imaging to investigate sequential changes of oral SCC in the 4NQO animal model. In this study, we could not differentiate benign hyperplastic lesions and early malignant lesions, such as, HGD or CIS by structural OCT imaging alone. This is because the change in the epithelium thickness or intactness of the basement membrane was similar in both processes. Although some studies have suggested that the thickness of the epithelium, intactness of basement membrane, intraepithelial intensity reduction, or optical scattering properties could

be a marker for differentiating benign and malignant oral lesions [17,37,38], these results have been contradicted by other studies [15,16]. The strength of our study is the use of vascular OCT to visualize microvascular changes in differentiating benign or malignant oral lesions; these have been used broadly for diagnosing early esophageal SCC, and were also studied initially in oral SCC [21–23].

Our results show the ability of the OCT system to detect IPCLs closed to 10  $\mu\text{m}$ . As normal tissue transforms to dysplasia and SCC, the caliber and shape of the IPCLs changed from small, uniform, and closed loops to dilated, open, and non-uniform loops (Fig. 7). These findings are consistent with those of a previous study using magnifying endoscopy and narrow-band imaging [21].

Versus commercialized magnifying endoscopy and narrow-band imaging, vascular OCT is less invasive, non-contact, easy to operate, and rapid, and offers a larger field of view and deeper penetration depth. This makes OCT more suitable for examinations of the oral cavity than magnifying endoscopy. The presentation of structural and vascular imaging at the same time offers a better evaluation of tumor invasion, which is still suboptimal under current IPCL classification. Moreover, the vascular OCT system can observe not only changes in the IPCLs but also changes in the deeper branching vessels in LP. After quantitative analysis of branching vessels, we found an increasing trend in vessel area density, median diameter, and bending in diseased tissue compared to a normal tongue. Although statistical analysis could not be performed in this study because of the small sample size, this quantitative method and information could be important for developing automatic identification in future OCT systems. Further studies with more samples are ongoing.

Another strong point of our study is the 4NQO animal model. Unlike the common polycyclic hydrocarbon 9,10 dimethyl-1,2, benzanthrane (DMBA) hamster model, the 4NQO model is the best available experimental system for investigating early oral SCC [28]. This model can be used to study different stages of cancer development, and progressive structural and vascular changes can be observed *in vivo* via OCT. This work also used a large and oriented tissue specimen for histological analysis, unlike the small and poorly oriented biopsy specimens in most human studies. The large and oriented tissue specimen offers the opportunity to study different cancerous stages at the same time. In our study, two mice had separate and different pathological changes in one resected specimen (Figs. 5 and 6). Thus, we could observe different structural and vascular OCT imaging concurrently, which showed the ability of vascular OCT to distinguish different pathological processes.

There were some limitations in this study. First, the lateral resolution was insufficient to clearly visualize normal IPCLs. Second, the algorithm used in this study used only the amplitude of OCT signals for angiography calculation; the method is not sensitive to both the axial and transverse blood flows. Third, shadowing artifacts originating from the regularly lined papilla may also decrease the detection sensitivity on the imaging of IPCLs. Fortunately, we can see the change of IPCLs clearly in a diseased tongue. This may be due to atrophic change or destruction of papilla in disease progression; thus, the artifacts decrease in the diseased stage. By increasing the system resolution, utilizing complex OCT signals for angiography calculation [39], and implementing a shadow removal method [40], the system sensitivity to image IPCLs can increase.

In summary, this study demonstrated the ability of structural and vascular OCT to be combined for diagnosing benign and early malignant oral lesions in an animal model. Subsequent studies with more samples and statistical analysis are currently under development. Obviously, validation in humans is still needed before clinical utility is established.

**Funding**

National Yang-Ming University SPARK project (MOST 105-2321-B-010-016); Taipei Veterans General Hospital-National Yang-Ming University Excellent Physician Scientists Cultivation Program (V107B-031).

**Disclosures**

The authors declare that there are no conflicts of interest related to this article.